



Original Article

Atmospheric controlled processing enabling highly textured NKN with enhanced piezoelectric performance

Lisheng Gao^a, Sinan Dursun^a, A. Erkan Gurdal^b, Eberhard Hennig^c, Shujun Zhang^d, Clive A. Randall^{a,*}

^a Department of Material Science & Engineering, Materials Research Institute, The Pennsylvania State University, University Park, PA, 16802, USA

^b Solid State Ceramics, Inc., State College, PA, 16803, USA

^c PI Ceramic GmbH, Lindenstrasse 07589, Lederhose, Germany

^d Institute for Superconducting & Electronic Materials, Australian Institute of Innovative Materials, University of Wollongong, Wollongong, NSW, 2522, Australia



ARTICLE INFO

Keywords:

Piezoelectrics

Lead-free

Textured

low pO_2 sintering

ABSTRACT

High-performance lead-free piezoelectrics are of interest as alternate materials to confront potential legislative actions on lifting the exemption on lead-based piezoelectric materials. In this work, we demonstrated a highly textured commercial-grade Li- and Ta- modified (Na, K)NbO₃ (NKN) lead-free piezoceramic that was sintered under low oxygen partial pressure (pO_2) atmospheres using the solid state template grain growth (TGG) method. It was found that a moderate low pO_2 condition not only facilitated the reactive template grain growth but also lowered the temperature required for such process. Highly textured NKN with a converse piezoelectric coefficient $d_{33}^* \approx 680 \text{ pm V}^{-1}$ was obtained, this remarkable piezoelectric property can be explained by the position of the polymorphic phase boundary of NKN. With considerations on both performance and cost, this work not only presented the potential for NKN to meet the requirement of commercial applications, but also provided an effective processing strategy to utilize low cost base metal inner electrodes in the future.

1. Introduction

Piezoelectric materials are the core for electromechanical applications such as multilayer actuators, piezoelectric transducers, energy harvesting, etc. [1] The piezoelectric industry traditionally has been taking advantage of the morphotropic phase boundary (MPB) design of Pb(Zr, Ti)O₃ PZT for its superior electromechanical properties, [2,3] and the PZT-based materials still dominate the market, based on cost and performance. Public recognition and concern over the hazardous materials have pushed the legislation to restrict the use of some chemistries and materials in electrical equipment, which becomes the driving force for discovery and development of the new materials that are eco-friendly. However, some exemptions are applied due to lack of reliable and appropriate substitutions. The lead-based electromechanical materials have been under the exemption of the RoHS (Restriction of Hazardous Substances Directive) by the European Union for years with a deadline set for the year 2020 [4]. Tremendous efforts have been made to discover and improve the lead-free piezoelectric materials [5].

(Na, K)NbO₃ (NKN), (Na, Bi)TiO₃ (NBT), and BaTiO₃ (BT) are well-known lead-free piezoelectric materials. Since Saito et al. [6] first

reported that the textured NKN could have comparable properties to a soft PZT, various strategies have been engaged to not only improve the piezoelectric properties of NKN, but also to improve the feasibility and control the cost of product fabrications, i.e. understand polymorphic phase boundaries (PPB) and their compositional design [7–13], mechanical structure design [14,15], and novel processing [16], using low cost base metal electrodes [17–20].

The piezoelectric properties of single crystal ferroelectric materials are typically much higher than that of the polycrystalline piezoceramics. Particularly, by taking advantage of the anisotropic feature and domain engineering in single crystals, Park and Shrout [21] reported giant piezoelectric coefficients ($> 2000 \text{ pC N}^{-1}$) were obtained in Pb(Zn_{1/3}Nb_{2/3})O₃-PbTiO₃. Saito et al. [6] reported piezoelectric strain coefficient $d_{33}^* \sim 750 \text{ pm V}^{-1}$ in $\langle 001 \rangle_{\text{PC}}$ textured NKN using plate-like NN templates. Work on texturing NKN has been reported by multiple researchers [22,23]; though excellent textured ceramics were obtained, the improvement in properties was limited. Until very recently, Jiang et al. [24,25] reported high piezoelectric performance in the single crystal NKN; Li et al. [26] reported textured NKN with ultrahigh d_{33}^* of $\sim 980 \text{ pm V}^{-1}$ in their $\langle 001 \rangle_{\text{PC}}$ oriented NKN ceramic. Besides, Textured Na_{0.5}Bi_{0.5}TiO₃-BaTiO₃ (NBT) based piezoelectric

* Corresponding author.

E-mail addresses: car4@psu.edu, randall@matse.psu.edu (C.A. Randall).

<https://doi.org/10.1016/j.jeurceramsoc.2018.12.047>

Received 5 November 2018; Received in revised form 19 December 2018; Accepted 20 December 2018

Available online 21 December 2018

0955-2219/© 2018 Elsevier Ltd. All rights reserved.

materials were studied as well. With the LOF > 90%, the piezoelectric performance of $< 001 >_{PC}$ orientated NBT was found to be enhanced under high electric fields [27,28].

Texturing technology using the templated grain growth (TGG) method has been investigated for adoption into the piezoelectric applications to enhance the piezoelectric responses that are being developed by Messing et al. [29] When templates are of the same composition as the matrix phase, which is called homoepitaxial TGG process, the grain growth is simply Ostwald Ripening [30]. However, templates that hold different chemical compositions but similar structure and lattice parameters can be used as well, and it is called heteroepitaxial TGG process. The only difference is that the matrix ceramic has to nucleate on the templates surface first during sintering; afterward, the grain growth undergoes Ostwald ripening. These processes were usually conducted at high temperature to offer the kinetic energies needed for grain boundary migrations. Furthermore, by purposely introducing the liquid phase, the kinetics can be expedited during sintering, and/or a lower temperature process can be performed. Lowering the processing temperature is important for those materials containing volatile elements, such as lead-based materials and alkaline elements-based materials. Tremendous efforts were made to control the loss of volatile elements, which include utilizing liquid phase to lower sintering temperature and shortening the annealing time, [31–34] and changing the oxygen partial pressure to limit the kinetics of volatilization [16,35], etc.

Multilayer structures are widely adopted into the piezoelectric applications to increase the overall response with much lower required operational voltage. Device fabrication and adoption are particularly sensitive to the cost. Metal electrodes count considerable volumetric fractions in the multilayer devices, and precious metals such as Ag, Pd, and Pt are still widely used as inner electrodes. Therefore, the potential cost of the metal electrodes has to be determined specifically while developing materials and processing. In particular, the feasibility of integrating lower cost base-metal inner electrodes, e.g., Cu and Ni, should be considered as an important factor for developing materials and processing strategies.

In this paper, we will report a comprehensive work on enhancing the piezoelectric properties by texturing commercial-grade NKN in controlled low pO_2 environments. Synthesis of $NaNbO_3$ templates and ceramic processing details will be presented, and possible mechanisms behind processing and the enhanced piezoelectric properties will be discussed.

2. Experimental section

2.1. $NaNbO_3$ (NN) plate-like templates preparation

Synthesis of $NaNbO_3$ (NN) platelets was performed via two steps, molten salt synthesis (MMS) and topochemical conversion method (TCM). In the first step, the molten salt method was used to synthesize $Bi_{2.5}Na_{3.5}Nb_5O_{18}$ (BiNN5) precursor platelet microcrystals. The starting chemicals are Na_2CO_3 (99.9%, Alfa Aesar), Bi_2O_3 (99.5%, Sigma Aldrich), and Nb_2O_5 (99.9%, Alfa Aesar). The raw chemicals were weighed according to the stoichiometric ratio of BiNN5. Then, the sodium chloride (NaCl) was added in accordance with a weight ratio of oxides to the salt of 1:1.5. The batched chemicals were ball milled for 24 h in ethanol. Afterward, dried powders were annealed at 1125°C for 6 h. The final BiNN5 precursor platelet microcrystals were washed multiple times with hot deionized water to remove the residual NaCl salt and Cl⁻ ion byproducts.

The obtained BiNN5 precursor platelets were used to produce NN platelet microcrystals by TCM. NaCl was added to the precursor with the double amount of the BiNN5. In addition, 50% excessive Na_2CO_3 was added at this step. Na_2CO_3 and NaCl were weighed and ball milled in ethanol for 24 h. This mixture was then added into a beaker and mixed with BiNN5. The mixture was dried and annealed at 975°C for 6 h.

The product was washed with hot deionized water multiple times to remove the residual salt. Finally, NN particles were washed with HNO_3 solution to remove the by-product Bi_2O_3 , followed by washing again with DI-water several times.

2.2. Fabrication of textured NKN

Tape casting method was adopted to prepare the bulk NKN ceramic disc samples. The initial NKN ceramic slurry was prepared, the detailed method and formula can be found elsewhere. [19] Then the slurry was transferred from the ball-milling bottle to a beaker with magnetic stirring bar. Plate-like $NaNbO_3$ templates were dispersed using Methyl Ethyl Ketone (MEK), the amount of the templates was 5 wt% of the NKN powder. The well-dispersed templates were added to the NKN slurry. The mixed slurry was stirred at room temperature for 4 h. The slurry was then defoamed on a slow rolling mill before tape casting. Doctor blade method was used to form the ceramic green tapes. The ceramic green tapes were cut into 2.54 cm by 2.54 cm squares, the stacked tapes were laminated at 75°C under an isostatic pressure of ~ 20MPa for 20 min. Disc-shaped samples were punched out of the laminated tapes. The NKN ceramic disc samples were burnt out and sintered under different conditions. Air-firing test was conducted first. The binder burnt-out NKN pellets were placed on an alumina substrate and covered by an alumina crucible. The crucible was sealed using alumina cement. Samples were sintered at 1050°C and 1100°C for 12 h, respectively.

The samples were also sintered under low partial pressures of oxygen, which were carried out in a tube furnace at 1050°C, under partial pressures of oxygen, with pO_2 of 10^{-6} atm, 10^{-7} atm, 10^{-8} atm, 10^{-9} atm, 10^{-10} atm, and 10^{-12} atm, respectively, for 12 h. NKN samples were also sintered at 1050°C for a different annealing time under 10^{-8} atm to investigate the evolution of texturing. The pO_2 was controlled by accurately flowing the mixture of wet N_2 (N_2 flow through ion-free water at 50°C), dry N_2 , and N_2/H_2 so-called save gas. The pO_2 was monitored by zirconia oxygen sensor (Superox, Super System INC. Cincinnati, OH). An optimized condition was confirmed at 1060°C under pO_2 of 10^{-8} atm for 4 h, followed by the re-oxidation procedure to fill the oxygen vacancies created during sintering.

2.3. Characterization

X-ray diffraction (PANalytical X'Pert Pro) data was taken to reveal the characteristic peaks of the perovskite NKN and calculate the degree of texture. Electron backscatter diffraction (EBSD) (Oxford Nordlys Max2) was adopted to obtain the crystal orientation mapping of the ceramics. The microstructure and grain morphology of the co-sintered samples were studied by both Scanning Electron Microscope (SEM) (ESEM FEI) and Transmission Electron Microscopy (TEM) (Titan, Talos, FEI). The chemical composition analysis was performed by using the electron micro probe analyzer (EPMA) (SXFiveFE, CAMECA). The samples were poled under 30 kV cm^{-1} for 10 min at 55°C normal to the tape-casting direction. The dielectric behavior was determined via the capacitance measured as a function of temperature using an LCR meter (HP4284A, Agilent Technologies Inc., Santa Clara, CA). The Polarization-Electric field (P-E) hysteresis was measured using a modified Sawyer-Tower circuit; a linear variable differential transformer (LVDT) was also coupled to this system to conduct strain-electric field measurements. A sinusoidal electric field was applied at 1 Hz with the maximum electric field of 30 kV cm^{-1} . The normalized strain coefficient d_{33}^* (S_{\max}/E_{\max}) was calculated at 20 kV cm^{-1} .

3. Results and discussion: ceramic processing

3.1. Plate-like $NaNbO_3$ templates

$NaNbO_3$ (NN) templates have been used for fabrication of $< 001 >$ oriented (K, Na) NbO_3 -based ceramics by a reactive templated grain

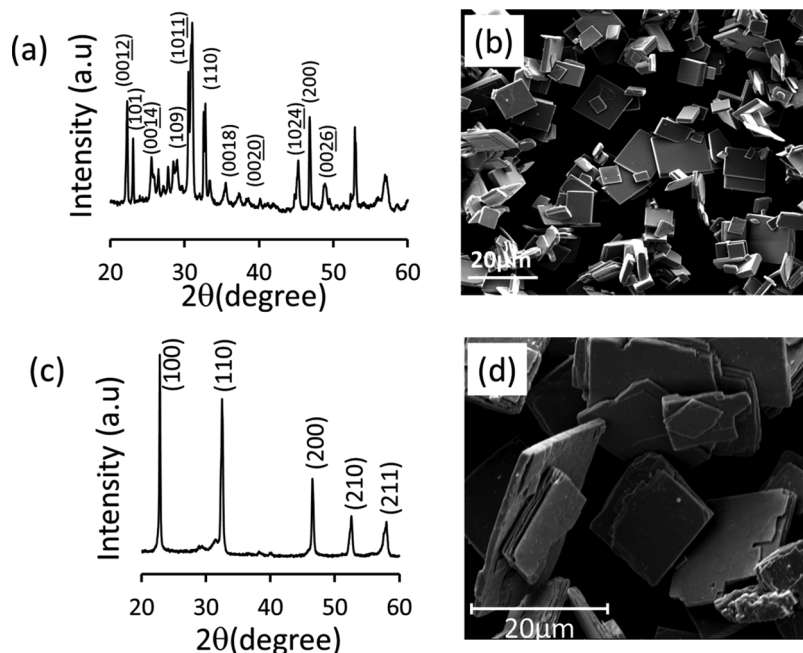


Fig. 1. X-ray diffraction pattern and scanning electron micrographs of (a) and (b) BNN5 precursor fabricate by molten salt synthesis at 1125 °C for 6 h and (c) and (d) NN template synthesized via topochemical conversion method at 975 °C for 6 h.

growth method [6]. NaNbO_3 templates were fabricated by a two-stage synthesis process. In the first stage, plate-like $\text{Bi}_{2.5}\text{Na}_{3.5}\text{Nb}_5\text{O}_{18}$ (BiNN5) particles were synthesized by the molten salt synthesis method according to Eq. (1). Fig. 1 (a) shows the XRD pattern and SEM micrograph of BiNN5 particles synthesized in NaCl molten salt at 1125 °C for 6 h. The XRD peaks were indexed in accordance with JCPDS card no. 42-0399. Almost all the diffraction peaks verified as BiNN5 . However, there were some minor peaks belonging to the phases BNN2 ($\text{Bi}_2\text{O}_2[(\text{Bi}_{0.5}\text{Na}_{0.5})\text{Nb}_2\text{O}_7]$), or BiNN4 Bi_2O_2 ($[(\text{Bi}_{0.5}\text{Na}_{2.5})\text{Nb}_4\text{O}_{13}]$). These phases are similar to those of BiNN5 , thus there was no adverse effect on the final product NN plate-like template in the second stage topochemical conversion. [36,37]. In addition, the XRD peaks of BiNN5 precursors provided $[\text{Bi}_2\text{O}_2]^{2+}$ layered perovskite structure, which exhibited a strong $[00l]$ orientation. Fig. 1(b) shows the SEM micrographs of BiNN5 precursors, exhibiting minimal agglomeration and nearly rectangular platelet shape with layered morphology. The particle size of BiNN5 precursors varied from 10 to 25 μm , with the thickness varied from 0.5 to 1 μm , suitable for synthesizing NN template at the second step by topochemical microcrystal conversion (TMC) method.

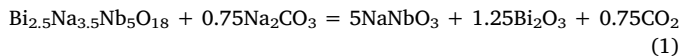
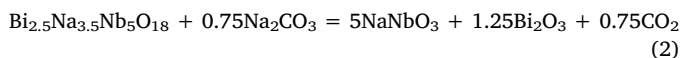


Fig. 1 (c) shows the XRD pattern of NN plate-like templates that were synthesized based on the chemical reaction given in Eq. (2), at 975 °C for 6 h. All diffraction peaks belonged to preferentially oriented perovskite structure with $(h00)$ peaks, demonstrating that the weakly bonded $-\text{Bi}_2\text{O}_2]^{2+}$ was possibly removed by heat treatment during the reaction, rather than replacing the Bi^{3+} with Na^+ . Finally, as shown in Fig. 1 (d), the layer-structured BiNN5 particles were converted into the pure perovskite NaNbO_3 possessing the same morphology as BiNN5 . It was noticed that small amount of residual Bi was detected in the earlier studies with no adverse effects on the TGG processes [36].



3.2. Low $p\text{O}_2$ sintered textured NKN

Lotgering Orientation Factor (LOF) [38] was used to evaluate the degree of texture. The LOF can be calculated based on Eq. (3) below, where F is the value of LOF;

$$F = \frac{P - P_0}{1 - P_0} \times 100\% \quad (3)$$

where P_0 and P can be calculated by Eqs. (4) and (5),

$$P_0 = \frac{\sum I_0(100)(00l)}{\sum I_0(hkl)} \quad (4)$$

$$P = \frac{\sum I(100)(00l)}{\sum I(hkl)} \quad (5)$$

where I_0 and I are the intensity of peaks from random orientated samples and orientated samples, respectively.

XRD spectra of textured Li- and Ta- modified NKN (hereafter NKN-T in the processing section) sintered in ambient air is shown in Fig. 2. It

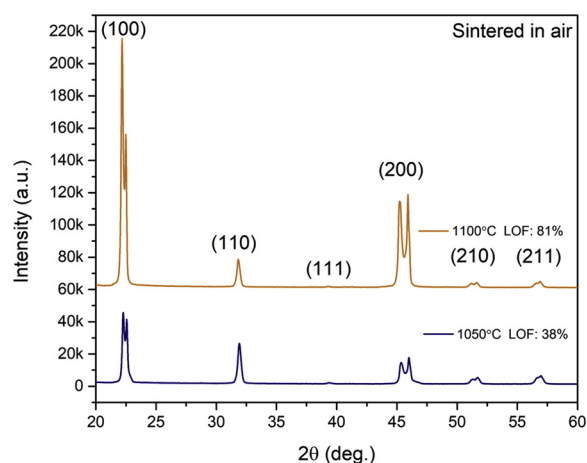


Fig. 2. XRD spectra of NKN sintered in ambient air at 1100 °C and 1050 °C for 12 h.

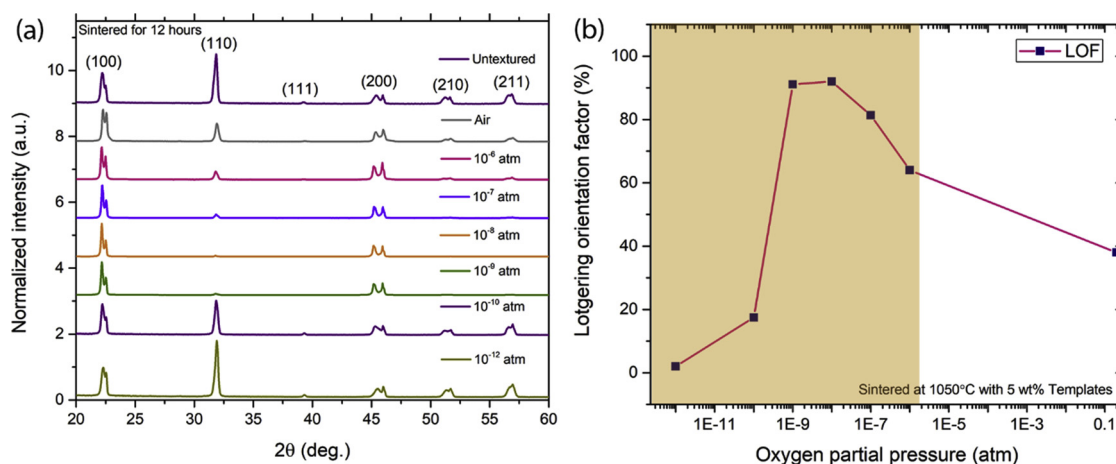


Fig. 3. (a) Normalized XRD spectra of NKN-T sintered at 1050 °C under different pO_2 conditions; (b) Lotgering orientation factor as a function of pO_2 from samples sintered at 1050 °C for 12 h. All peaks are indexed based on prototype cubic perovskite structure.

was found that sintering temperature played an important role in texturing in the air atmosphere. The Lotgering orientation factor (LOF) was found to be about ~38% in NKN samples that were sintered at 1050 °C for 12 h. However, with 50 °C elevation of sintering temperature, the LOF showed a significant increase to ~83%. Though the NKN was texturable in the air, they showed high dielectric loss values (> 20%) after such long-time heat treatment due to the highly volatile alkaline elements.

XRD spectra of NKN-T sintered under different atmospheric conditions were plotted and are shown in Fig. 3 (a), compared with the randomly oriented NKN (NKN-R); the intensity was normalized based on the intensity of the (100)_{PC} peaks. For low pO_2 sintering, samples were first sintered under pO_2 of 10^{-6} atm, and the LOF of ~65% was obtained. By decreasing the pO_2 , LOF increased up to ~95% at pO_2 of 10^{-8} atm. Further decreasing the sintering pO_2 to 10^{-9} atm led to a slightly lower LOF value of ~90%, which dramatically decreased to ~17% for the sample sintered under pO_2 of 10^{-10} atm. The samples sintered under pO_2 of 10^{-12} atm were barely textured. Fig. 3 (b) shows the LOF as a function of the sintering pO_2 with sintering time of 12 h. Of particular interest is that the maximum LOF was obtained within the pO_2 region that is compatible with co-firing with copper metal electrodes. This region (that is compatible with copper co-firing) is marked with orange shadow in Fig. 3 (b) for sintering at 1050 °C.

Fig. 4 shows the *ex-situ* XRD spectra of NKN-T that were sintered at 1050 °C under 10^{-8} atm for different dwelling time. As shown in Fig. 4 (a), it was found that the intensity of non-{h00}_{PC} peaks gradually decreased with sintering time. Eventually, the non-{h00}_{PC} peaks were barely visible in the spectra. In randomly orientated NKN, the (110)_{PC} peak usually have the highest intensity; therefore, looking at intensity change of (110)_{PC} peaks would be a direct method to observe the progress of the texturing. Close inspection of (110)_{PC} peak around 31.8° and the split (200)_{PC} peaks around 45.2°/46.0° was shown in Fig. 4 (b) and (c), respectively. A crystallographic evolution of the NKN-T was observed with the increase of the texture degree. The intensity of (110)_{PC} peaks was found to decrease with the sintering time, indicating the crystallographic orientation alignment occurred during the heat treatment, as shown in Fig. 4 (b). Fig. 4 (c) shows the peaks corresponding to (200)_{PC} peaks. In the orthorhombic phase, the (200)_{PC} peaks split into (002) and (200) peaks. The piezoelectric properties of NKN are sensitive to the polymorphic phase boundary; usually the orthorhombic phase and tetragonal phase of NKN can be roughly distinguished by the intensity of the (002) and (200) peaks. [39–41] In orthorhombic phase, the ratio between (002) and (200) peak should be 2:1, and such ratio would be 1:2 in tetragonal phase. It was found that with increasing the texture degree, the (002)/(200) peak ratio decreased to close to 1. Such evolution of {200} peaks suggested mixed

orthorhombic and tetragonal phases in the NKN-T prior to poling.

EBSD was adopted to further consider the quality of textured NKN, offering a direct visualization of the orientation through the inversed pole figure maps. A large quantity of grains were studied to obtain the macroscopic texture information. The EBSD graphs are shown in Fig. 5. Fig. 5(a) shows the mapping from NKN-R, with its corresponding inversed pole figure mapping in Fig. 5 (c). It was observed that low maximum multiples uniform pole density (MUD), with a narrow range in the NKN-R. Besides, the signal was picked up at all directions, indicating that the orientation of the grains was distributed randomly without preference in the NKN-R as to be expected. Fig. 5 (b) shows the maps of the surface of NKN-T, the color in this maps consists of dominantly red and green, which represents the reflection from {001} planes. In the inversed pole figure graphs shown in Fig. 5 (e), high MUD, up to 26.77 from the {001} planes with low MUD, down to 0.05, from all other none {001} planes suggested that the NKN-T was well textured along the < 001 > directions.

3.3. Microstructure characterization

The fracture surfaces of the NKN-T sintered under different pO_2 conditions are shown in Fig. 6. The arrow indicates the tape casting direction. Fig. 6 (a) shows the cross-section of the NKN-T sintered in the air; both large square-shaped and small grains were observed. The large grains were from the heteroepitaxial growth on the NN seeds. Fig. 6 (b) showed the fracture surface of NKN sintered at a pO_2 of 10^{-8} atm; the grains grew significantly with square-shaped morphology, and there is a needle-shaped cavity in the center of this giant grains. Facets of the grains were generally parallel to the tape casting directions. The needle-shaped cavities in the center of the grains were associated with the residual NaNbO₃ templates. The templates were well aligned along the tape casting direction in the NKN-T. The disappearance of the pre-placed templates suggested that it could have dissolved into the NKN matrix during sintering. Fig. 6 (c) showed the fracture surface of the NKN-T sintered at pO_2 of 10^{-10} atm. Smaller grains are found in the ceramic sintered under these conditions, suggesting that the low pO_2 environment hindered the texturing process significantly.

4. Discussion

The XRD spectra in Fig. 3, and also in Fig. 6, shows the micrographs of the fractured surface of NKN sintered under the different sintering conditions. It is noted that under appropriate pO_2 atmospheric conditions, there is improved texturing quality relative to the typical air sintering conditions; meanwhile, a higher degree of texture can be easily achieved at more moderate sintering conditions, e.g. lower

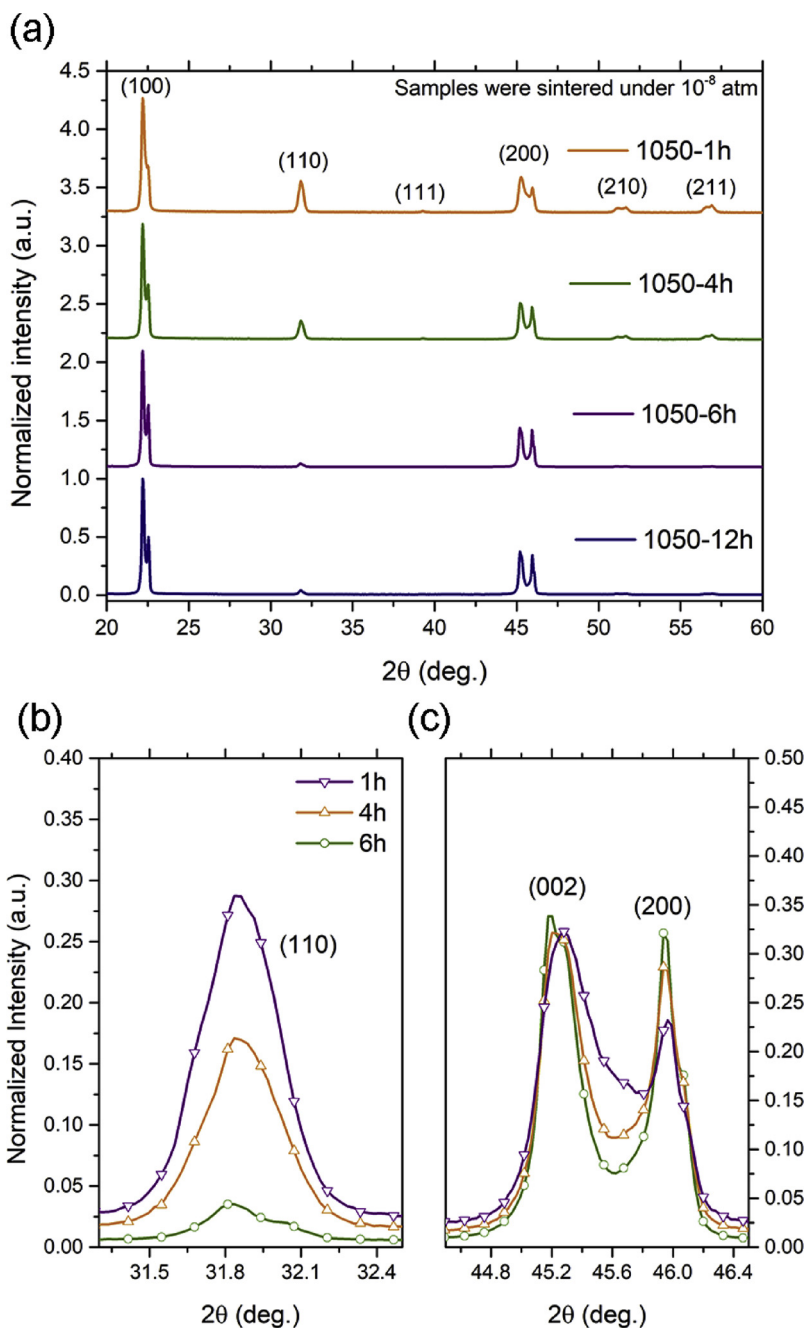


Fig. 4. (a) Normalized XRD spectra of NKN-T sintered at 1050 °C under pO_2 of 10^{-8} atm for different time durations; (b) (100) peak and (c) (002)/(200) peaks of NKN-T sintered for 1 h, 4 h, and 6 h, respectively. Peaks are indexed based on prototype cubic perovskite structure.

temperature and shorter dwelling time. The NKN has relatively lower volatility of the alkaline elements, especially potassium, under lower oxygen partial pressures. [42] Therefore low pO_2 sintering suppressed the volatility of the alkaline elements in NKN, limiting the bimodal grain growth in NKN [17,43]. However, bimodal grain size distribution was observed in the samples with low texture degree. Here, the matrix was compositionally different from the templates, hence heteroepitaxial TGG. As seen in Fig. 6, the grain growth during texturing the NKN could undergo discontinuous grain growth; [44] $NaNbO_3$, as a small amount nuclei, grew rapidly by consuming the small NKN-matrix grains, and eventually dissolved into the matrix due to the chemical difference.

Oxygen partial pressure played an important role in this study, where the different degree of texture and microstructure were observed in the samples sintered under different atmospheric conditions. Jung et al. [43] reported that in an environment of pO_2 above 10^{-17} atm,

grain growth behavior was suppressed in $BaTiO_3$, while Shimizu et al. [16] observed suppressed grain growth in $NaNbO_3$ as well. Grain growth involves bulk diffusion and grain-boundary oxygen transport. [45] Both the formation of liquid phase and dissolution of the seeds and matrix can significantly expedite the diffusion rate [46]. In addition, oxygen transport also played an important role during the grain growth [43,45]. Logically, air sintering gives a high concentration of oxygen along grain boundaries, which thus leads to fast grain growth due to the high kinetics of oxygen transport [43]. However, the result was not as expected. In addition to facilitating the grain growth, the environmental oxygen couples with the alkaline elements and diffuses to sample surface, then evaporates into the surrounding environment. Therefore, competition exists between condensation and volatilization, which undercut the grain growth behavior. Shigemi and Wada [47,48] found that an oxygen deficient environment could reduce the volatility

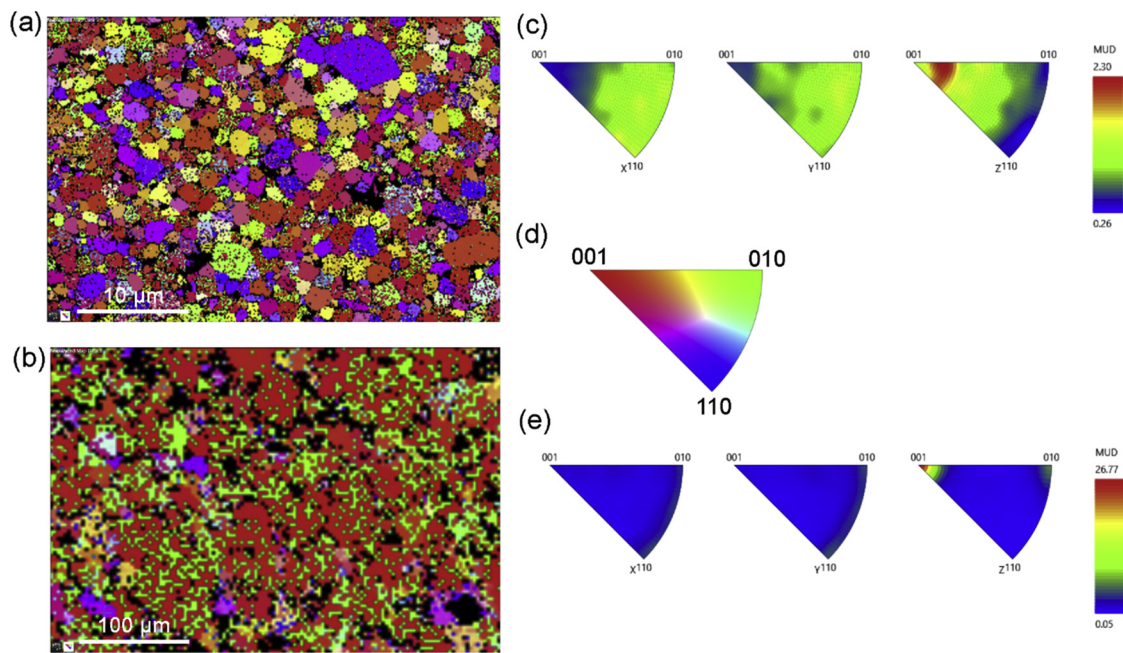


Fig. 5. EBSD orientation mapping, (a) and (b) color contrast mapping of random orientated and textured NKN ceramics; (c) and (e) shows the inverse pole figure with MUD data corresponding to (a) and (b), respectively; (d) color codes show the crystallographic direction oriented out of the surface of the images in (a) and (b).

of the alkaline elements. Here, low pO_2 environment retarded the oxygen transport activities along the grain boundaries, resulting in the slower kinetics of the thermodynamically favored volatilization. Consequently, liquid phase formation and volatilization were under control during the sintering, hence allowing for continual grain growth, responsible for the highly textured NKN with well grown and oriented grains. Further decreasing the pO_2 resulted in insufficient oxygen to produce liquid phase, thus significantly suppressed the grain growth. Therefore, a low degree of texture was observed due to the slow kinetics.

5. Electrical properties

Textured NKN that was sintered under an optimized condition was used for electrical property investigation. Hereafter, it will be represented as NKN-1060 T.

5.1. Effect from poling to crystallography

Ex-situ XRD spectra of the NKN-1060 T are illustrated in Fig. 7; spectra of the virgin state and poled state are both presented in Fig. 7

(a), showing clear difference on both $(100)_{PC}$ and $(200)_{PC}$ peaks. Fig. 7 (b) showed the $(110)_{PC}$ peaks of NKN in both states. It was found that the intensity of $(110)_{PC}$ peaks decreased after poling, suggesting the poling process artificially changed the domain configurations and induced domain wall motions. Details of the $(002)_{PC}$ and $(200)_{PC}$ peaks are shown in Fig. 7 (c); the ratio between (002) and (200) peaks was increased to 2:1. It primarily suggested that the poling process leads to a higher fraction of orthorhombic phase. [7,40,49–51] Furthermore, the enhanced lower angle (002) peak revealed that the lattice had the higher d-spacing planes dominantly perpendicular to the applied electric field, showing that the majority of the dipoles were aligned during poling.

5.2. Domain structures

Detailed microstructures of the NKN-1060 T were investigated by TEM and are shown in Fig. 8. Fig. 8 (a) shows the high-resolution TEM image of NKN along the $\langle 110 \rangle_{PC}$ zone axis; the atomic arrangement is consistent with high crystallization quality of the NKN-1060 T. Fig. 8 (b) and (c) show the bright field and dark field images of the lamellar domain structure of the poled NKN samples, respectively; Fig. 8 (d) presents the corresponding selected area electron diffraction (SAED)

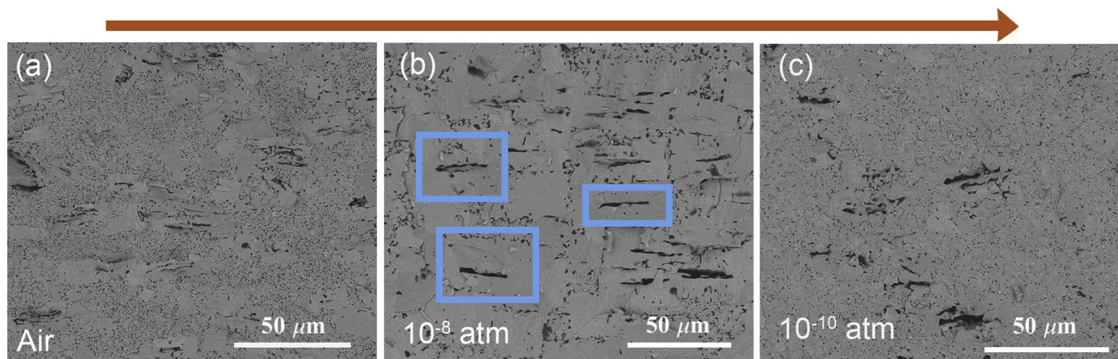


Fig. 6. Fracture surface of NKN-T sintered at 1050 °C for 12 h under different conditions. sintered (a) under ambient air condition, (b) under pO_2 of 10^{-8} atm, blue squares indicated the shape of the large grains, (c) under pO_2 of 10^{-10} atm. Orange colored arrow showed the tape casting direction. (For interpretation of the references to colour in this figure legend, the reader is referred to the web version of this article.)

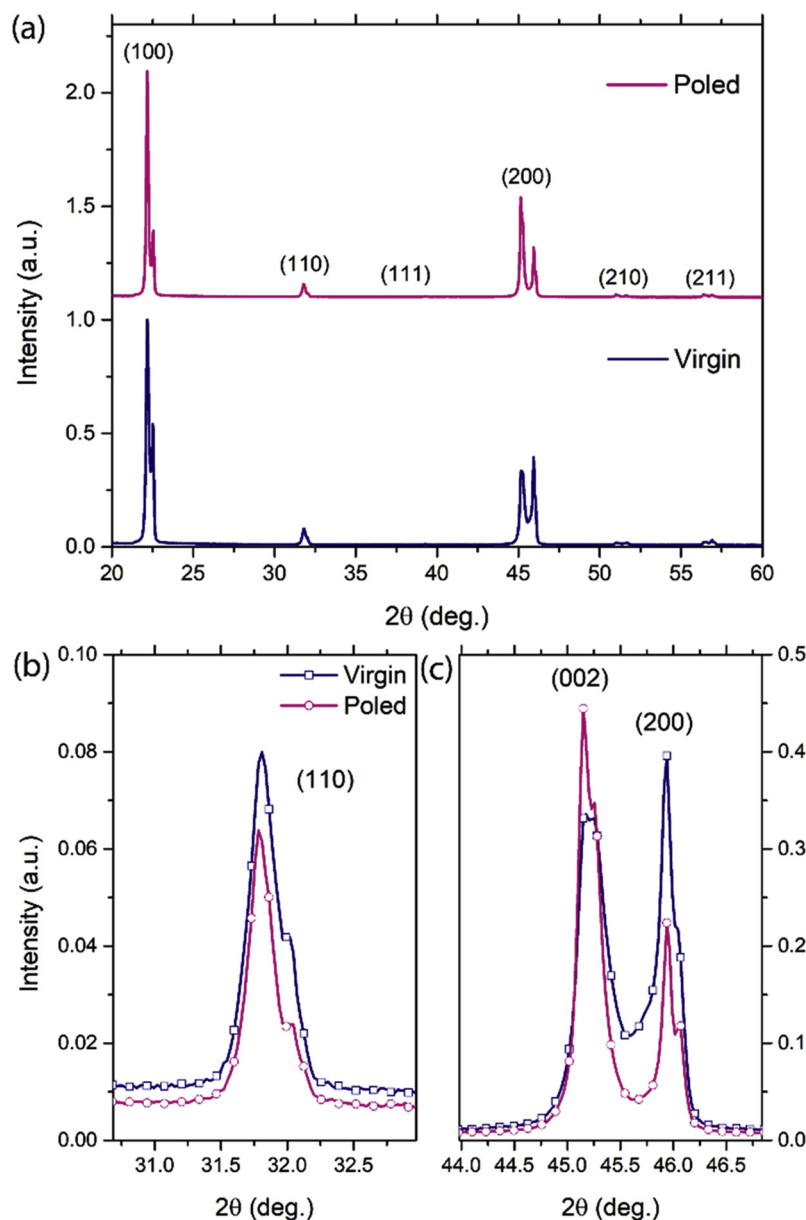


Fig. 7. XRD spectra of virgin and poled NKN-1060 T, (a) full spectra of the NKN, (b) close view of (110) peaks, (c) Close view of (002)/(200) peaks. Peaks are indexed based on prototype cubic perovskite structure.

pattern, which is along the $\langle 001 \rangle_{\text{PC}}$ zone axis. The domain structures were collected from the cross-section area of NKN samples. Dominated $\{110\}_{\text{PC}}$ domain walls were observed in the poled NKN ceramics, which could be assigned to both 60° and 90° domain walls. Fig. 8 (c) illustrates a close view of the dark field image of the area in the green box in Fig. 8 (b) to better present the domain structures. Fig. 8 (e) shows the dark field domain structures of a NKN-1060 T sample prepared in a different batch, with the SAED pattern along $\langle 001 \rangle_{\text{PC}}$ zone axis shown in Fig. 8 (f). Identical $\{110\}_{\text{PC}}$ type domain structures were observed.

5.3. Dielectric and piezoelectric properties

Dielectric properties of the NKN-1060 T over 35°C – 450°C were measured and given in Fig. 9. Fig. 9 (a) shows the dielectric constant as a function of the temperature for NKN-1060 T. The inset in Fig. 9 (a) showed data collected from an NKN-R that was sintered under the same condition. For both NKN-1060 T and NKN-R, the dielectric anomalies

were found at $\sim 326^\circ\text{C}$, attributed to the phase transition temperature from ferroelectric/tetragonal to the paraelectric/cubic phase of this type NKN. A small dielectric hump was found at $\sim 70^\circ\text{C}$ in the NKN-R, due to the polymorphic phase transition between orthorhombic and tetragonal phase transition. But this peak was further smeared and not able to be clearly spotted in the NKN-1060 T. Such a change was expected to be associated with the chemical composition change due to the dissolution of the NN seeds into the NKN matrix. It was proved by studying the composition through EPMA, K and Na are volatile and soluble to water, thus were not used as criteria. Change of Ta/Nb ratio was used to understand the impact from NaNbO_3 templates. The atomic ratio decreased from 0.232 to 0.218 by adding the templates, indicating and further proved that the templates dissolved and then altered the composition. Multiple works [7,52] reported that $T_{\text{O-T}}$ of NKN could be lowered and smeared by adding Li and Ta. Skidmore et al. [11] demonstrated the phase diagram of the Li and Ta modified NKN, which suggested that the smeared $T_{\text{O-T}}$ range was extremely sensitive to the composition when it was tuned below 100°C . However, the Curie

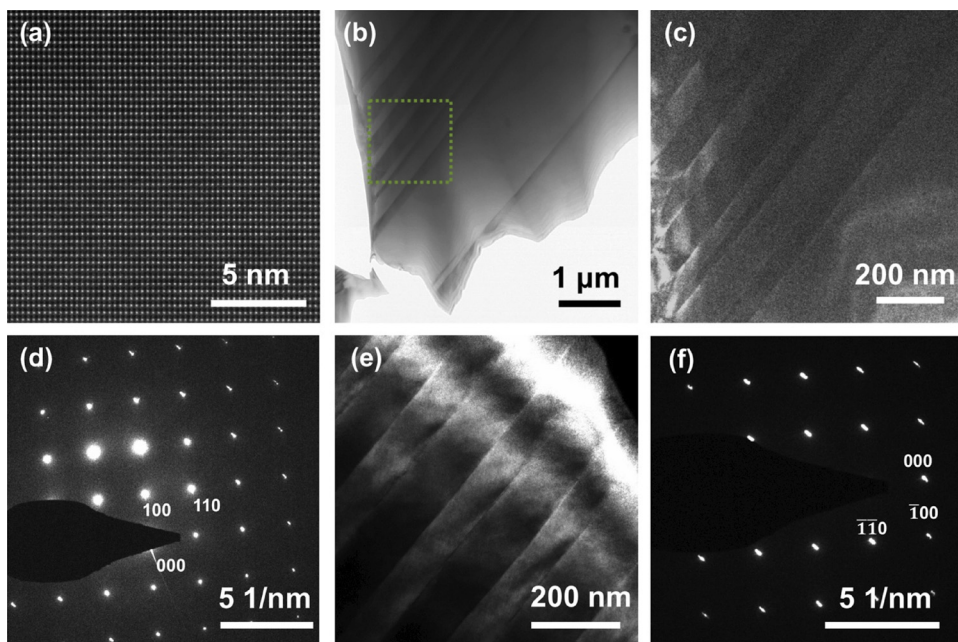


Fig. 8. Microstructure of NKN-1060 T under TEM, (a), high resolution TEM along $\langle 110 \rangle$ zone axis; (b) bright field, (c) detailed dark field domain structures of the green box in (b); (d) SAED diffraction pattern along $\langle 100 \rangle$ zone axis corresponding to the TEM microstructure in (b) and (c); (e) dark field domain structure observed from a different-batch sample, (f) SAED diffraction pattern along $\langle 100 \rangle$ zone axis corresponding to (e). (For interpretation of the references to colour in this figure legend, the reader is referred to the web version of this article.)

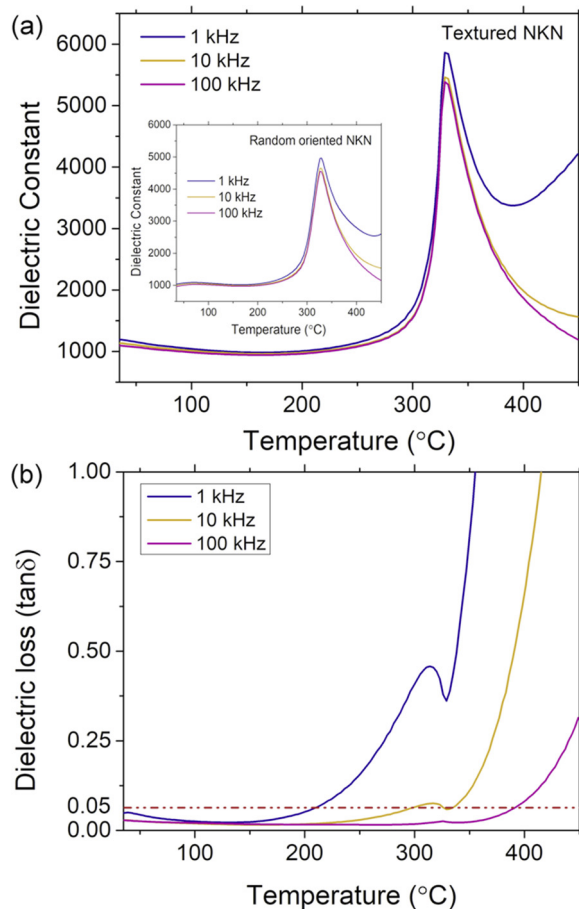


Fig. 9. Dielectric properties of NKN-1060 T, (a) dielectric constant as a function of temperature, the inset shows the data from NKN-R sintered under the same condition; (b) dielectric loss as a function of temperature.

temperature was not as sensitive as the T_{O-T} to the subtle change in terms of increasing or decreasing the concentration of both Li and Ta together. [9] The dielectric loss as a function of the temperature for NKN-1060 T is shown in Fig. 9 (b), remaining below 5% until 200 °C,

which potentially increased the operational temperature range for the NKN-1060 T.

High field performance from both NKN-1060 T and NKN-R is shown in Fig. 10. As seen in Fig. 10 (a), bipolar P-E loops were collected with sinusoidal AC field at 1 Hz from the non-polarized samples. Well saturated, typical ferroelectric hysteresis loops were observed in both NKN-1060 T and NKN-R [53]. In the NKN-1060 T, the remanent polarization (P_r) was found to be $\sim 14.3 \mu\text{C cm}^{-2}$, with the coercive field (E_c) of $\sim 10.0 \text{ kV cm}^{-1}$. The P_r and E_c of the NKN-R were $20.0 \mu\text{C cm}^{-2}$ and 8.1 kV cm^{-1} , respectively. It was not clear the mechanism behind the drop of the P_r , but the composition of the NKN could have played a significant role. The dissolution of NN templates could move the composition slightly away from the polymorphic phase boundary, thus causing the change. Bipolar P-E hysteresis loops that were collected up to 60 kV cm^{-1} of the NKN-1060 T are illustrated in Fig. 10 (b), where saturation polarization (P_{sat}) is $\sim 20.3 \mu\text{C cm}^{-2}$, by reading the intercept of the extrapolation of the saturated polarization. The well saturated high field P-E loop demonstrated the extraordinary quality of the textured NKN ceramics. The unipolar strain versus electric field plots of both NKN-1060 T and NKN-R are shown in Fig. 10 (c). A piezoelectric coefficient d_{33}^* of $\sim 680 \text{ pm V}^{-1}$ was achieved from the NKN-1060 T. Compared with the d_{33}^* value of $\sim 380 \text{ pm V}^{-1}$ from NKN-R, textured NKN significantly increased the converse piezoelectric response of the NKN. Some of the important parameters of both NKN-1060 T and NKN-R were listed in Table 1. As known, the d_{33}^* of commercially available PZT-4 is $\sim 700 \text{ pm V}^{-1}$ [1]; the $\langle 001 \rangle_{PC}$ textured NKN in this study presented a comparable d_{33}^* value to the lead-base material.

6. Conclusions

Plate-like NaNbO_3 templates were successfully synthesized using the molten salt method. Through alternating the extra NaCO_3 batched, the quality of the templates was able to be controlled. The commercial-grade Li- and Ta- modified NKN was successfully textured along $\langle 001 \rangle_{PC}$ using TGG method. It was found that the atmosphere condition could remarkably influence the texturing quality for NKN. Although higher sintering temperature in the air significantly increased the degree of texture, in the low pO_2 atmosphere, the highly oriented NKN was able to be obtained at lower temperatures under pO_2 of 10^{-8} atm. Such atmospheric condition was suitable for co-firing with base metal copper electrodes. Compared with the NKN-R, the d_{33}^* was

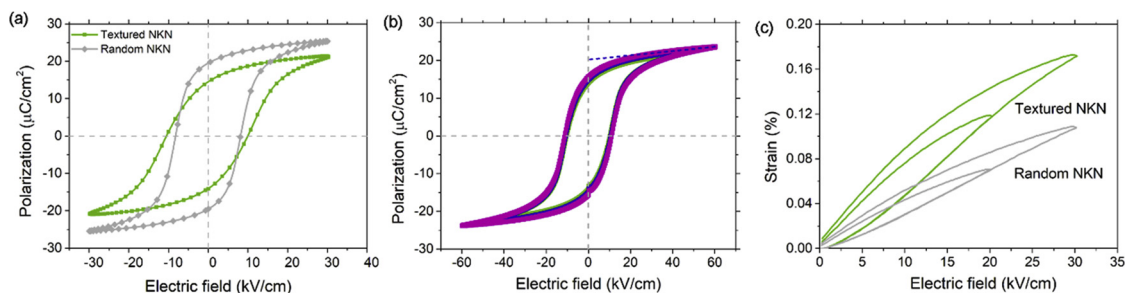


Fig. 10. Bipolar P-E hysteresis loops of (a) NKN-R and NKN-1060 T with the maximum electric field of 30 kV cm^{-1} , (b) high-field bipolar P-E hysteresis loops of NKN-1060 T, (c) unipolar S-E of both NKN-R and NKN-1060 T.

Table 1

Important dielectric, ferroelectric, and piezoelectric properties of the NKN-R and NKN-1060 T.

	Dielectric constant (poled)	$\tan\delta$	E_c (pm V^{-1})	P_r ($\mu\text{C cm}^{-2}$)	d_{33} (pC N^{-1})	d_{33}^* (pm V^{-1})
NKN-R	970	0.02	8	20	220	380
NKN-1060T	810	0.03	10	14	270	680

significantly improved from $\sim 380 \text{ pm V}^{-1}$ to $\sim 680 \text{ pm V}^{-1}$ by texturing the NKN along $\langle 001 \rangle_{\text{PC}}$ orientation. All in all, the success of fabrication of textured NKN under low $p\text{O}_2$ opened the door for fabricating Cu co-fired multilayer piezoelectric devices, which would significantly lower the cost on the metal electrodes for multilayer piezoelectric applications.

Acknowledgments

The Authors would like to thank Amanda Baker, Steve Perini, and Jeff Long for their dedicated work on maintaining the lab and providing technical assistance, Thank you for Julie Anderson for her assistance on collecting EBSD data. Thanks to Dr. Minoru Ryu and Dr. Ke Wang for their help on TEM. Thanks for PI Ceramic GmbH for providing high-quality NKN ceramic powder and Empower Materials for providing high-quality QPAC-40 binder polymer. This material is based upon work supported in part by the National Science Foundation, as part of the Center for Dielectrics and Piezoelectrics under Grant Nos. IIP-1361571 and 1361503.

References

- [1] B. Jaffe, W.R. Cook, H.L. Jaffe, *Piezoelectric Ceramics*, Academic Press, 1971.
- [2] G. Shirane, A. Takeda, Phase transitions in solid solutions of PbZrO_3 and PbTiO_3 (I) small concentrations of PbTiO_3 , *J. Phys. Soc. Japan* 7 (1952) 5–11, <https://doi.org/10.1143/JPSJ.7.5>.
- [3] G. Shirane, K. Suzuki, A. Takeda, Phase transitions in solid solutions of PbZrO_3 and PbTiO_3 (II) X-ray study, *J. Phys. Soc. Japan* 7 (1952) 12–18, <https://doi.org/10.1143/JPSJ.7.12>.
- [4] The European Parliament and the Council of the European Union, Directive 2011/65/EU of the European Parliament and of the Council of 8 June 2011 on the restriction of the use of certain hazardous substances in electrical and electronic equipment, *Off. J. Eur. Union Stud.* 54 (2011) 88–110 (accessed October 11, 2015), <http://www.rohsguide.com/>.
- [5] T.R. Shrout, S.J. Zhang, Lead-free Piezoelectric Ceramics: Alternatives for PZT? *J. Electroceram.* 19 (2007) 111–124, <https://doi.org/10.1007/s10832-007-9047-0>.
- [6] Y. Saito, H. Takao, T. Tani, T. Nonoyama, K. Takatori, T. Homma, T. Nagaya, M. Nakamura, Lead-free piezoceramics, *Nature* 432 (2004) 84–87, <https://doi.org/10.1038/nature03028>.
- [7] Y. Guo, K. Kakimoto, H. Ohsato, $(\text{Na}_{0.5}\text{K}_{0.5})\text{NbO}_3\text{-LiTaO}_3$ lead-free piezoelectric ceramics, *Mater. Lett.* 59 (2005) 241–244, <https://doi.org/10.1016/j.matlet.2004.07.057>.
- [8] Y. Guo, K. Kakimoto, H. Ohsato, Dielectric and piezoelectric properties of lead-free $(\text{Na}_{0.5}\text{K}_{0.5})\text{NbO}_3\text{-SrTiO}_3$ ceramics, *Solid State Commun.* 129 (2004) 279–284, <https://doi.org/10.1016/j.ssc.2003.10.026>.
- [9] Y. Saito, H. Takao, High performance lead-free piezoelectric ceramics in the $(\text{K},\text{Na})\text{NbO}_3\text{-LiTaO}_3$ solid solution system, *Ferroelectrics* 338 (2006) 17–32, <https://doi.org/10.1080/00150190600732512>.
- [10] M.S. Kim, S. Jeon, D.S. Lee, S.J. Jeong, J.S. Song, Lead-free NKN-5LT piezoelectric materials for multilayer ceramic actuator, *J. Electroceram.* 23 (2009) 372–375, <https://doi.org/10.1007/s10832-008-9470-x>.
- [11] T.A. Skidmore, T.P. Comyn, A.J. Bell, F. Zhu, S.J. Milne, Phase diagram and structure-property relationships in the lead-free piezoelectric system: $\text{Na}_{0.5}\text{K}_{0.5}\text{NbO}_3\text{-LiTaO}_3$, *IEEE Trans. Ultrason. Ferroelectr. Freq. Control* 58 (2011) 1819–1825, <https://doi.org/10.1109/TUFFC.2011.2019>.
- [12] S. Zhang, R. Xia, T.R. Shrout, G. Zhang, J. Wang, Characterization of lead free $(\text{K}_{0.5}\text{Na}_{0.5})\text{NbO}_3\text{-LiSbO}_3$ piezoceramic, *Solid State Commun.* 141 (2007) 675–679, <https://doi.org/10.1016/j.ssc.2007.01.007>.
- [13] J.B. Lim, S. Zhang, J.-H. Jeon, T.R. Shrout, $(\text{K},\text{Na})\text{NbO}_3$ -based ceramics for piezoelectric “hard” lead-free materials, *J. Am. Ceram. Soc.* 93 (2010) 1218–1220, <https://doi.org/10.1111/j.1551-2916.2009.03528.x>.
- [14] K. Uchino, S. Takahashi, Multilayer ceramic actuators, *Curr. Opin. Solid State Mater. Sci.* 1 (1996) 698–705, [https://doi.org/10.1016/S1359-0286\(96\)80054-4](https://doi.org/10.1016/S1359-0286(96)80054-4).
- [15] C.A. Randall, A. Kelnberger, G.Y. Yang, R.E. Eitel, T.R. Shrout, High strain piezoelectric multilayer actuators - a material science and engineering challenge, *J. Electroceram.* 14 (2005) 177–191, <https://doi.org/10.1007/s10832-005-0956-5>.
- [16] H. Shimizu, K. Kobayashi, Y. Mizuno, C.A. Randall, Advantages of low partial pressure of oxygen processing of alkali niobate: NaNbO_3 , *J. Am. Ceram. Soc.* 97 (2014) 1791–1796, <https://doi.org/10.1111/jace.12815>.
- [17] K. Kobayashi, Y. Doshida, Y. Mizuno, C.A. Randall, Possibility of cofiring a nickel inner electrode in a $(\text{Na}_{0.5}\text{K}_{0.5})\text{NbO}_3\text{-LiF}$ piezoelectric actuator, *Jpn. J. Appl. Phys.* 52 (2013) 09KD07, <https://doi.org/10.7567/JJAP.52.09KD07>.
- [18] S. Kawada, M. Kimura, H. Hayashi, K. Ogiso, T. Konoike, H. Takagi, Study of nickel inner electrode lead-free piezoelectric ceramics, 2011 Int. Symp. Appl. Ferroelectr. 2011 Int. Symp. Piezoresponse force microsc, *Nanoscale Phenom. Polar Mater. ISAF/PPM 2011* 3 (2011) 1–4, <https://doi.org/10.1109/ISAF.2011.6014102>.
- [19] L. Gao, S.-W. Ko, H. Guo, E. Hennig, C.A. Randall, Demonstration of Copper Co-Fired $(\text{Na},\text{K})\text{NbO}_3$ Multilayer Structures for Piezoelectric Applications, *J. Am. Ceram. Soc.* 99 (2016) 2017–2023, <https://doi.org/10.1111/jace.14207>.
- [20] L. Gao, H. Guo, S. Zhang, C.A. Randall, Base metal co-fired multilayer piezoelectrics, *Actuators* 5 (2016) 8, <https://doi.org/10.3390/act5010008>.
- [21] S.-E. Park, T.R. Shrout, Ultrahigh strain and piezoelectric behavior in relaxor based ferroelectric single crystals, *J. Appl. Phys.* 82 (1997) 1804, <https://doi.org/10.1063/1.365983>.
- [22] W. Ge, J. Li, D. Viehland, Y. Chang, G.L. Messing, Electric-field-dependent phase volume fractions and enhanced piezoelectricity near the polymorphic phase boundary of $(\text{K}_{0.5}\text{Na}_{0.5})_{1-x}\text{Li}_x\text{NbO}_3$ textured ceramics, *Phys. Rev. B* 83 (2011) 224110, <https://doi.org/10.1103/PhysRevB.83.224110>.
- [23] H. Zhang, Y. Zhu, P. Fan, M.A. Marwat, W. Ma, K. Liu, H. Liu, B. Xie, K. Wang, J. Koruza, Temperature-insensitive electric-field-induced strain and enhanced piezoelectric properties of textured $(\text{K},\text{Na})\text{NbO}_3$ -based lead-free piezoceramics, *Acta Mater.* 156 (2018) 389–398, <https://doi.org/10.1016/j.actamat.2018.07.005>.
- [24] M. Jiang, C.A. Randall, H. Guo, G. Rao, R. Tu, Z. Gu, G. Cheng, X. Liu, J. Zhang, Y. Li, Seed-free solid-state growth of large lead-free piezoelectric single crystals: $(\text{Na}_{1/2}\text{K}_{1/2})\text{NbO}_3$, *J. Am. Ceram. Soc.* 98 (2015) 2988–2996, <https://doi.org/10.1111/jace.13723>.
- [25] J. Zhang, M. Jiang, G. Cheng, Z. Gu, X. Liu, J. Song, L. Li, Y. Du, Microstructure, Piezoelectric, Ferroelectric and dielectric properties of $\text{Na}_{0.5}\text{K}_{0.5}\text{NbO}_3$ single crystals prepared by seed-free solid-state crystal growth, *Ferroelectrics* 502 (2016) 210–220, <https://doi.org/10.1080/00150193.2016.1236235>.
- [26] P. Li, J. Zhai, B. Shen, S. Zhang, X. Li, F. Zhu, X. Zhang, Ultrahigh piezoelectric properties in textured $(\text{K},\text{Na})\text{NbO}_3$ -based lead-free ceramics, *Adv. Mater.* 30 (2018) 1705171, <https://doi.org/10.1002/adma.201705171>.
- [27] H. Yilmaz, G.L. Messing, S. Trolier-McKinstry, (Reactive) templated grain growth of textured sodium bismuth titanate $(\text{Na}_{1/2}\text{Bi}_{1/2}\text{TiO}_3\text{-BaTiO}_3)$ ceramics—I processing, *J. Electroceram.* 11 (2003) 207–215, <https://doi.org/10.1023/B:JECE.0000026375.50590.81>.
- [28] H. Yilmaz, S. Trolier-McKinstry, G.L. Messing, (Reactive) templated grain growth of textured sodium bismuth titanate $(\text{Na}_{1/2}\text{Bi}_{1/2}\text{TiO}_3\text{-BaTiO}_3)$ ceramics—II dielectric and piezoelectric properties, *J. Electroceram.* 11 (2003) 217–226, <https://doi.org/10.1023/B:JECE.0000026376.48324.21>.
- [29] G.L. Messing, S. Trolier-McKinstry, E.M. Sabolsky, C. Duran, S. Kwon, B. Brahmarouti, P. Park, H. Yilmaz, P.W. Rehrig, K.B. Eitel, E. Suvaci, M. Seabaugh, K.S. Oh, Templated grain growth of textured piezoelectric ceramics, *Crit. Rev. Solid State Mater. Sci.* 29 (2004) 45–96, <https://doi.org/10.1080/10408430490490905>.
- [30] P.W. Voorhees, The theory of Ostwald ripening, *J. Stat. Phys.* 38 (1985) 231–252,

- <https://doi.org/10.1007/BF01017860>.
- [31] J.G. Fisher, A. Benčan, J. Holc, M. Kosec, S. Vernay, D. Rytz, Growth of potassium sodium niobate single crystals by solid state crystal growth, *J. Cryst. Growth* 303 (2007) 487–492, <https://doi.org/10.1016/j.jcrysgro.2007.01.011>.
- [32] T. Hayashi, T. Hasegawa, Piezoelectric properties of low-temperature sintered $\text{Pb}_{0.95}\text{Ba}_{0.05}[(\text{Mg}_{1/3}\text{Nb}_{2/3})_{0.125}\text{Zr}_{0.445}\text{Ti}_{0.43}]\text{O}_3$ ceramics with chemically-added LiBiO_2 sintering aid, *J. Eur. Ceram. Soc.* 25 (2005) 2437–2441, <https://doi.org/10.1016/j.jeurceramsoc.2005.03.078>.
- [33] H.J. Hwang, K. Watari, M. Sando, M. Toriyama, K. Niihara, Low-temperature sintering and high-strength $\text{Pb}(\text{Zr}, \text{Ti})\text{O}_3$ -matrix composites incorporating silver particles, *J. Am. Ceram. Soc.* 80 (1997) 791–793.
- [34] N.J. Donnelly, T.R. Shrout, C.A. Randall, The role of Li_2CO_3 and PbO in the low-temperature sintering of Sr, K, Nb (SKN)-Doped PZT, *J. Am. Ceram. Soc.* 92 (2009) 1203–1207, <https://doi.org/10.1111/j.1551-2916.2009.03073.x>.
- [35] N.J. Donnelly, C.A. Randall, Pb loss in $\text{Pb}(\text{Zr}, \text{Ti})\text{O}_3$ ceramics observed by in situ ionic conductivity measurements, *J. Appl. Phys.* 109 (2011) 104107, <https://doi.org/10.1063/1.3585831>.
- [36] Y. Yan, D. Liu, W. Zhao, H. Zhou, H. Fang, Topochemical synthesis of a high-aspect-ratio platelet NaNbO_3 template, *J. Am. Ceram. Soc.* 90 (2007) 2399–2403, <https://doi.org/10.1111/j.1551-2916.2007.01818.x>.
- [37] Y. Chang, Z. Yang, X. Chao, Z. Liu, Z. Wang, Synthesis and morphology of anisotropic NaNbO_3 seed crystals, *Mater. Chem. Phys.* 111 (2008) 195–200, <https://doi.org/10.1016/j.mchemphys.2008.04.031>.
- [38] F.K. Lotgering, Topotactical reactions with ferrimagnetic oxides having hexagonal crystal structures—I, *J. Inorg. Nucl. Chem.* 9 (1959) 113–123, <https://doi.org/10.15713/ins.mmj.3>.
- [39] A. Martin, K. Kakimoto, K. Hatano, Y. Doshida, K.G. Webber, Ferroelastic behavior across the orthorhombic-to-tetragonal phase transition region of NKN-based lead-free ferroelectrics, *J. Appl. Phys.* 122 (2017) 204102, <https://doi.org/10.1063/1.4989759>.
- [40] H. Guo, S. Zhang, S.P. Beckman, X. Tan, Microstructural origin for the piezoelectricity evolution in $(\text{K}_{0.5}\text{Na}_{0.5})\text{NbO}_3$ -based lead-free ceramics, *J. Appl. Phys.* 114 (2013) 154102, <https://doi.org/10.1063/1.4825213>.
- [41] T.A. Skidmore, S.J. Milne, Phase development during mixed-oxide processing of a $[\text{Na}_{0.5}\text{K}_{0.5}\text{NbO}_3]_{1-x}[\text{LiTaO}_3]_x$ powder, *J. Mater. Res.* 22 (2007) 2265–2272, <https://doi.org/10.1557/jmr.2007.0281>.
- [42] P. Bomlai, P. Wichianrat, S. Muensit, S.J. Milne, Effect of calcination conditions and excess alkali carbonate on the phase formation and particle morphology of $\text{Na}_{0.5}\text{K}_{0.5}\text{NbO}_3$ powders, *J. Am. Ceram. Soc.* 90 (2007) 1650–1655, <https://doi.org/10.1111/j.1551-2916.2007.01629.x>.
- [43] Y.-I. Jung, S.-Y. Choi, S.-J.L. Kang, Effect of oxygen partial pressure on grain boundary structure and grain growth behavior in BaTiO_3 , *Acta Mater.* 54 (2006) 2849–2855, <https://doi.org/10.1016/j.actamat.2006.02.025>.
- [44] M. Hillert, On the theory of normal and abnormal grain growth, *Acta Metall.* 13 (1965) 227–238, [https://doi.org/10.1016/0001-6160\(65\)90200-2](https://doi.org/10.1016/0001-6160(65)90200-2).
- [45] R.L. Coble, Sintering crystalline solids. II. Experimental test of diffusion models in powder compacts, *J. Appl. Phys.* 32 (1961) 793–799, <https://doi.org/10.1063/1.1736108>.
- [46] D.F.K. Hennings, R. Janssen, P.J.L. Reynen, Control of liquid-phase-Enhanced discontinuous grain growth in barium titanate, *J. Am. Ceram. Soc.* 70 (1987) 23–27, <https://doi.org/10.1111/j.1151-2916.1987.tb04847.x>.
- [47] A. Shigemitsu, T. Wada, Enthalpy of formation of various phases and formation energy of point defects in perovskite-type NaNbO_3 by first-principles calculation, *J. Appl. Phys.* 43 (2004) 6793–6798, <https://doi.org/10.1143/JJAP.43.6793>.
- [48] A. Shigemitsu, T. Wada, Evaluations of phases and vacancy formation energies in KNbO_3 by first-principles calculation, *J. Appl. Phys.* 44 (2005) 8048–8054, <https://doi.org/10.1143/JJAP.44.8048>.
- [49] C. Liu, P. Liu, K. Kobayashi, W. Qu, C.A. Randall, Enhancement of piezoelectric performance of lead-free NKN-based ceramics via a high-performance Flux- $\text{NaF-Nb}_2\text{O}_5$, *J. Am. Ceram. Soc.* 96 (2013) 3120–3126, <https://doi.org/10.1111/jace.12461>.
- [50] M. Ichiki, L. Zhang, M. Tanaka, R. Maeda, Electrical properties of piezoelectric sodium-potassium niobate, *J. Eur. Ceram. Soc.* 24 (2004) 1693–1697, [https://doi.org/10.1016/S0955-2219\(03\)00475-8](https://doi.org/10.1016/S0955-2219(03)00475-8).
- [51] K. Wang, J.-F. Li, Domain engineering of lead-free Li-modified $(\text{K}, \text{Na})\text{NbO}_3$ polycrystals with highly enhanced piezoelectricity, *Adv. Funct. Mater.* 20 (2010) 1924–1929, <https://doi.org/10.1002/adfm.201000284>.
- [52] E. Hollenstein, M. Davis, D. Damjanovic, N. Setter, Piezoelectric properties of Li- and Ta-modified $(\text{K}_{0.5}\text{Na}_{0.5})\text{NbO}_3$ ceramics, *Appl. Phys. Lett.* 87 (2005) 182905, <https://doi.org/10.1063/1.2123387>.
- [53] J.F. Scott, Ferroelectrics go bananas, *J. Phys. Condens. Matter* 20 (2008) 021001, <https://doi.org/10.1088/0953-8984/20/02/021001>.